PHYSICAL CHEMISTRY

Crystallization-induced emission enhancement: A novel fluorescent Au-Ag bimetallic nanocluster with precise atomic structure

Tao Chen,[1,2] Sha Yang,[1,2] Jinsong Chai,[1,2] Yongbo Song,[1,2] Jiqiang Fan,[1,2] Bo Rao,[1,2] Hongting Sheng,[1,2]* Haizhu Yu,[1,2]* Manzhou Zhu[1,2]*

We report the first noble metal nanocluster with a formula of $Au_4Ag_{13}(DPPM)_3(SR)_9$ exhibiting crystallization-induced emission enhancement (CIEE), where DPPM denotes bis(diphenylphosphino)methane and HSR denotes 2,5-dimethylbenzenethiol. The precise atomic structure is determined by x-ray crystallography. The crystalline state of Au_4Ag_{13} shows strong luminescence at 695 nm, in striking contrast to the weak emission of the amorphous state and hardly any emission in solution phase. The structural analysis and the density functional theory calculations imply that the compact C–H···π interactions significantly restrict the intramolecular rotations and vibrations and thus considerably enhance the radiative transitions in the crystalline state. Because the noncovalent interactions can be easily modulated via varying the chemical environments, the CIEE phenomenon might represent a general strategy to amplify the fluorescence from weakly (or even non-) emissive nanoclusters.

INTRODUCTION

Noncovalent interactions (such as hydrogen bonding, π-π stacking, and cation-π interactions) are ubiquitous in solid-state materials, biological structures, and organic molecules (*1*, *2*). To date, the fascinating effect of the noncovalent interactions in dominating the physicochemical properties has attracted increasing research interests (*3*, *4*). Specifically, with the recent progress of optical imaging and sensing, noncovalent interaction–induced luminescence has been extensively explored for high structural flexibility, ease of adaptability, and good reversibility (*5*). In this context, fluorescent regulation (quenching or enhancement) has been successfully achieved for both macromolecules [such as nanosheets/biological structures (*6*, *7*)] and small molecules [such as pure organic luminogens (*8*)]. This effect has never been reported for the atomically precise, ultrasmall noble metal nanoclusters (MNCs), which are the structural bridge between individual atoms and mesosized nanoparticles.

In the past decades, ultrasmall MNCs (*9*–*13*), typically with core sizes smaller than 2 nm, have attracted considerable interest for their fascinating molecular-like physicochemical properties [for example, magnetism (*14*, *15*), chirality (*16*–*18*), and optoelectronics (*19*–*21*)]. Benefiting from low toxicity and good biocompatibility, luminescent MNCs have recently emerged as highly attractive materials, especially for biological imaging and sensing applications (*22*). Nonetheless, most of the reported luminescent MNCs are polydispersed materials or mixtures with variable compositions. The preparation of monodispersed fluorescent MNCs with precise atomic structure has long been challenging.

The precise atomic structure is fundamentally important in exploring structure-property relationships and the future design of more powerful materials. So far, several luminescent MNCs with precise structures determined by single-crystal x-ray crystallography have been reported (*23*–*30*). For example, Wang *et al.* (*23*) recently synthesized successfully a series of Ag_xAu_{25-x} alloy nanoclusters (NCs) and found that doping the 13th Ag atom significantly enhances the fluorescence quantum yield (QY) by ~200 times. Similarly, another Au-Ag alloy NC (that is, $Ag_{24}Au$) was reported by Bootharaju and co-workers to show over 25 times luminescence enhancement compared to the Ag_{25} NC (*27*). Meanwhile, our group found that Au_2Cu_6 NCs exihibit strong red emission, whereas neither Cu nor Au precursors are fluorescent. For these MNCs, the aggregation-induced emission mechanism has been proposed to account for the enhancement (*31*), in which the restriction of the rotation/vibration (*32*, *33*) acts as the main driving force for photoluminescence. Thus, both the composition/structure of the metal core and the ligand shell are critical. However, the metal-metal and metal-ligand interactions all correspond to strong bonding interactions. By contrast, the weak interaction induced photoemission, which has been frequently observed in small molecules and macromolecules, has not been reported for MNCs.

Herein, a novel Au-Ag bimetallic NC co-protected by thiolate and phosphine ligands has been sucessfully synthesized. The precise structure was elucidated by x-ray crystallography, and the formula is $Au_4Ag_{13}(DPPM)_3(SR)_9$, where DPPM denotes bis(diphenylphosphino) methane and HSR denotes 2,5-dimethylbenzenethiol. The four-Au–doped icosahedral M_{13} (that is, Au_4Ag_9) kernel in this NC is protected by three AgS_2P and one AgS_3 motifs. The Au_4Ag_{13} NC exhibits a unique crystallization-induced emission enhancement (CIEE) effect (Fig. 1), that is, the crystalline state shows strong luminescence at 695 nm, whereas the amorphous state (obtained via drying the CH_2Cl_2 solution of the Au_4Ag_{13} crystals) is weakly emissive, and the solution has essentially no emission. After careful analysis, we found that the CIEE effect is mainly caused by highly restricted vibrations and rotations in the crystalline state (*34*–*37*). In detail, both the triblade fan configuration of the framework and the C–H···π interactions contribute to the structural restrictions. This study sheds light on a general strategy to amplify the fluorescence of weakly emissive NCs by taking advantage of the readily available weak interactions in the assembled NCs.

RESULTS AND DISCUSSION

The $Au_4Ag_{13}(DPPM)_3(SR)_9$ NC was prepared by a one-pot method (see details in Materials and Methods). Briefly, a methanol solution of

[1]Department of Chemistry and Centre for Atomic Engineering of Advanced Materials, Anhui University, Hefei, Anhui 230601, P. R. China. [2]AnHui Province Key Laboratory of Chemistry for Inorganic/Organic Hybrid Functionalized Materials, Anhui University, Hefei, Anhui 230601, P. R. China.
*Corresponding author. Email: sht_anda@126.com (H.S.); yuhaizhu@ahu.edu.cn (H.Y.); zmz@ahu.edu.cn (M.Z.)

$AgNO_3$ was first mixed with $HAuCl_4{\cdot}3H_2O$ in CH_2Cl_2. After that, DPPM and HSR were added and then $NaBH_4$ was added, resulting in an immediate formation of the raw product. Finally, after washing with methanol three times, dissolving in CH_2Cl_2/ether, and recrystallization, red crystals were obtained in the crystallization (CCDC 1544143).

The structure of the $Au_4Ag_{13}(DPPM)_3(SR)_9$ NC was determined by x-ray crystallography. Each unit cell contains four pairs of enantiomers (see fig. S1 for the entire unit cell). Figure 2 shows the structure of one pair of enantiomers, and Fig. 3 shows the framework of the clockwise enantiomer.

As shown in Figs. 2 and 3, the structure consists of an icosahedral Au_4Ag_9 kernel, three AgS_2P, and one AgS_3 staple motifs. The four Au atoms occupy the icosahedral center and three symmetric sites on the icosahedral shell. Meanwhile, each Au atom on the icosahedral shell binds with one P atom of the bidentate DPPM ligands, whereas the other P atom of DPPM ligates with another Ag atom on the staple motif. Aside from the phosphine ligation, two thiolate ligands are also connected to satisfy the electronic and steric environments of the staple Ag atoms. The three AgS_2P motifs adopt the same configuration (Fig. 3). The Ag–S bond lengths range from 2.451 to 2.549 Å (2.500 Å in average), and the Ag–P bond lengths are all 2.410 Å. In addition to the structural motifs, the remaining four Ag atoms constitute a tetrahedral structure, with one Ag atom located on the C_3 symmetric axis of the remaining three Ag atoms on the icosahedral shell. This final Ag atom is symmetrically surrounded by the three S atoms of the thiolate ligands, constituting an AgS_3 motif. Here, each Ag–S bond in AgS_3 is 2.544 Å in length, and the S–Ag–S angle is 119.61° (Fig. 3). The entire single-crystal structure adopts a C_3 point group, and the three AgS_2P motifs constitute a triblade fan configuration. According to the direction of the triblade fan configuration, the enantiomers are classified into one clockwise and one anticlockwise structure (Fig. 2).

We used x-ray photoelectron spectroscopy (XPS) to analyze the electronic states of the metal atoms in the Au_4Ag_{13} NC. From Fig. 4, the Au 4f peak is higher than that of Au(0) (84.8 eV versus 84.0 eV), indicating the oxidation state of the Au atoms. The Ag 3d peak is higher than that of Ag(0) (368.5 eV versus 367.9 eV), indicating that the Ag atoms are negatively charged. Therefore, the XPS analysis implies the partial charge transfer from Au to Ag, and the reason for this anti-galvanic reduction might relate to the enhanced reducing ability within the very small MNCs (*38*). The similar Au→Ag electron transfer has also been observed in the recently reported $Au_{15}Ag_3(SR)_{14}$ (*39*). The product was further characterized by thermogravimetric analysis (TGA). A weight loss of 52.03% was observed (Fig. 5A), which is consistent with the theoretical loss of 52.16% for $Au_4Ag_{13}(DPPM)_3(SR)_9$.

The optical properties of the Au_4Ag_{13} NC were then investigated. From Fig. 5B, it can be seen that the Au_4Ag_{13} NCs display three absorption peaks (260, 330, and 430 nm) and one weak shoulder peak at 540 nm. To explore the electronic characteristics, time-dependent density functional theory (TD-DFT) calculations (*40*, *41*) were carried out. Meanwhile, Kohn-Sham (KS) molecular orbitals (MOs) were calculated to analyze the compositions of the frontier orbitals (Fig. 5C). The two methyl groups on the thiolate ligand were simplified with H atoms to reduce the computational cost, and the full details of the calculation methods are provided in the Supplementary Materials.

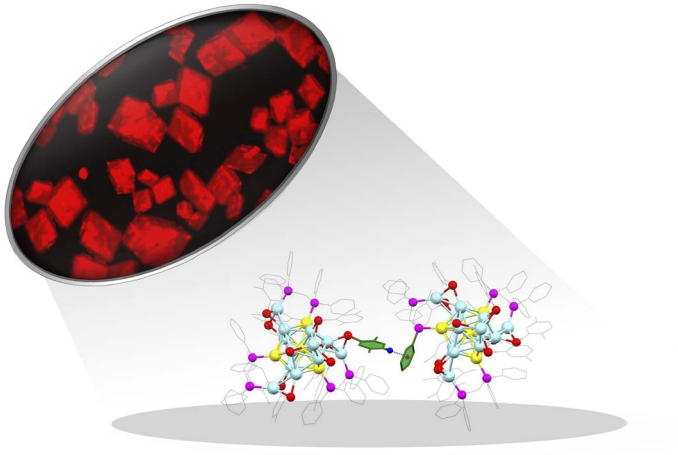

Fig. 1. Optical microscopy image of the fluorescent $Au_4Ag_{13}(DPPM)_3(SR)_9$ NCs and the key C–H···π interactions.

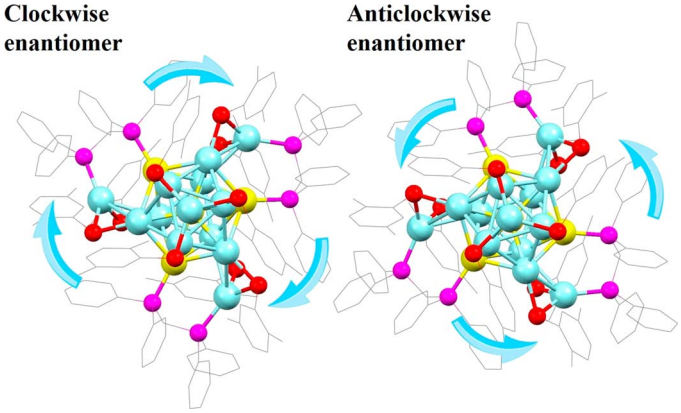

Fig. 2. The structure of one pair of enantiomers. Color labels: Ag, light blue; Au, yellow; P, magenta; S, red; C, gray; all H atoms are omitted.

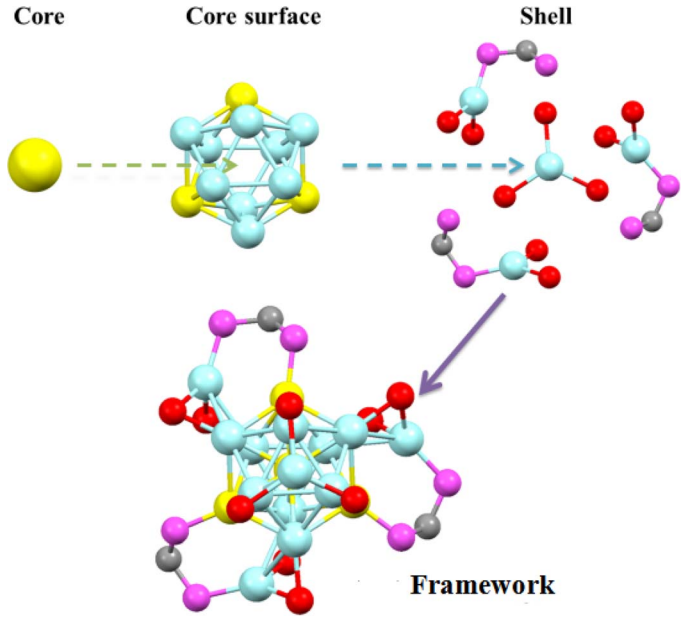

Fig. 3. The framework of the Au_4Ag_{13} NC. Color labels: Ag, light blue; Au, yellow; P, magenta; S, red; C, gray; all other carbon (except the bridging carbon atoms between two P atoms in DPPM) and hydrogen atoms are omitted.

Despite the systematic red shift of the theoretical absorption peaks (*42*–*45*), the overall profile is consistent with the experimental one. The first band on ultraviolet-visible (UV-vis) (~750 nm) corresponds to the highest occupied molecular orbital (HOMO)→lowest unoccupied molecular orbital (LUMO) transition. According to the KS orbital analysis (*46*–*48*), the HOMO is mainly constituted by the π-conjugations of the thiolate groups on the AgS_3 motif, whereas the main contribution of LUMO comes from the Ag(5sp) and Au(6sp) atomic orbitals in

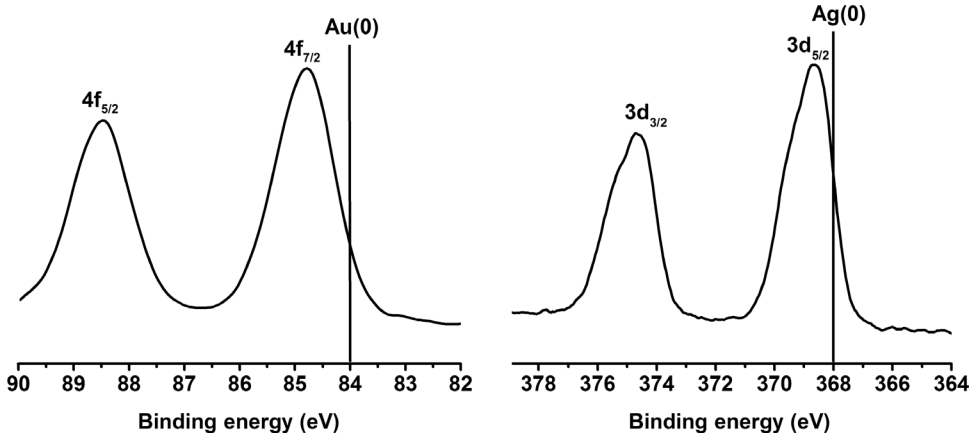

Fig. 4. Au 4f XPS spectrum and Ag 3d XPS spectrum.

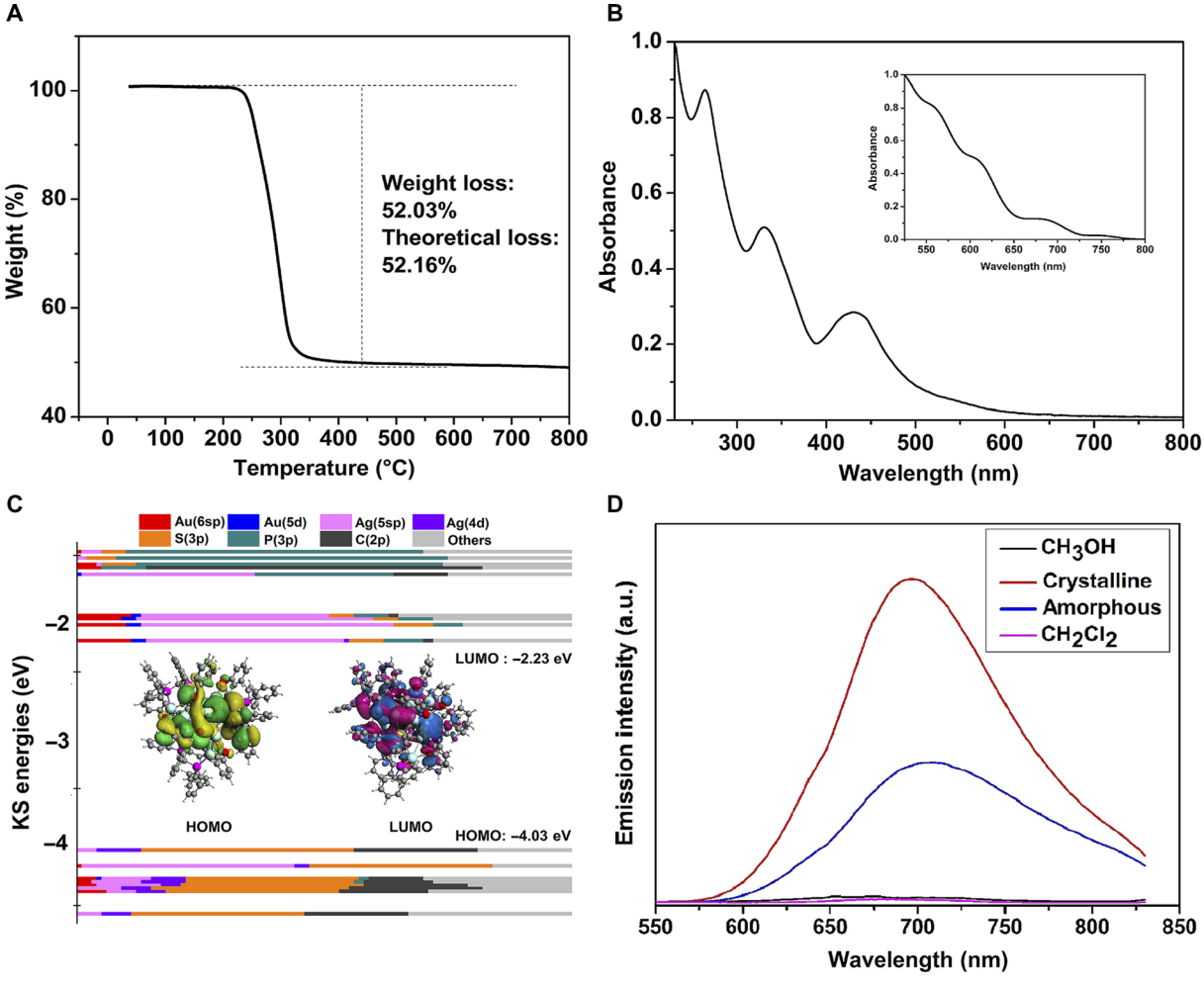

Fig. 5. Characterization of the $Au_4Ag_{13}(DPPM)_3(SR)_9$ NC. (**A**) TGA of the Au_4Ag_{13} NCs. (**B**) UV-vis spectrum of the Au_4Ag_{13} NCs in CH_2Cl_2 and theoretical spectrum with TD-DFT methods (inset). (**C**) KS MOs of the Au_4Ag_{13} NC. (**D**) Emission spectra of the crystalline (red line), solution (magenta line for CH_2Cl_2 and black line for MeOH solvent), and amorphous states (blue line) with excitation at 500 nm. a.u., arbitrary units.

the core surface (Fig. 5C). Therefore, the HOMO→LUMO transition is mainly the ligand-to-metal charge transfer (LMCT). Meanwhile, the second band (~680 nm) mainly corresponds to the transition of HOMO to LUMO+3 and LUMO+4. Because of the similar orbital compositions of LUMO+3/+4 to that of LUMO, the transition here is also mainly the π→sp transition (LMCT). By contrast, the former two bands (~540 and 600 nm) on the theoretical UV-vis mainly correspond to the transition from the lower two HOMOs (that is, HOMO−1/HOMO−2) to the upper LUMOs (LUMO+8 and LUMO+12 for the third band and LUMO+8 and LUMO+17 for the fourth band). To this end, the sp→sp interband transition mainly accounts for these two bands.

The photoluminescence of the CH_2Cl_2 solution of Au_4Ag_{13} is very weak (QY = 4.1×10^{-5} in fig. S2) and so is that of the MeOH solution (Fig. 5D). These observations are in sharp constrast to the UV-vis light–stimulated strong emissions of the as-prepared NCs observed during the synthetic processes (fig. S3). The crystalline state of Au_4Ag_{13} shows strong red emission (fig. S4) with a maximal emission wavelength of ~695 nm in the fluorescence spectrum (Fig. 5D). Meanwhile, the lifetime of the solution and crystalline state is 3.31 and 0.65 ns, respectively (fig. S5, A and B). For comparison, the amorphous state of Au_4Ag_{13} generated by the evaporation of CH_2Cl_2-dissolved Au_4Ag_{13} crystal (or by grinding the solid-state crystal) exhibits relatively weak fluorescence, and the maximal wavelength red shifts by 10 nm when compared to that of the crystalline state. Both the weakened intramolecular π-π stacking interactions (*35*) and the smaller torsion angle (*49*, *50*) of aromatic rings in the less regulated amorphous state (compared to the crystalline state) might account for the spectroscopic red shift. The fluorescence quantum efficiency (Φ_f) of the amorphous and the crystalline state is 1.14 and 2.68%, respectively.

The CIEE phenomenon in the Au_4Ag_{13} NC is remarkable, and such a phenomenon has not been reported for MNCs before. Because the N_2-bubbled solution shows the same optical phenomenon as the normal solution, the possibility of the interference of oxygen (in solution/amorphous state) could be eliminated. After carefully examining the structure of the Au_4Ag_{13} NCs, we noticed some unusual structural features. First, the overall framework is in a triblade fan configuration (Fig. 6A). According to recent studies on luminescent small molecules, such a structure is capable of restricting the vibrational/rotational movement during the electronic transitions and thus altering the optical properties (*51*). We anticipate that such a structural restriction is mainly responsible for the photoluminescence of the amorphous state. Nonetheless, this effect is unable to explain the significantly enhanced photoemission in the crystalline state compared to that of the amorphous state. To this end, we noticed that the spacing between each group of enantiomers is unnecessarily narrow, especially the distance between the -SPh on one enantiomer and the $-PPh_2$ groups on its neighboring enantiomer (Fig. 1). In detail, the distances between the hydrogen atom (para to the S atom) of the thiolate ligand and the centroid of the nearby phenyl ring of the DPPM ligand range from 2.564 to 2.573 Å (2.568 Å on average; fig. S6). The distances remind us of the C–H···π interactions, and these weak interactions are widely spread in the entire crystal structure. As shown in Fig. 6B, each single crystal consists of six groups of C–H···π interactions with the nearby enantiomers. The C–H bonds exclusively come from the phenyl groups of the thiolate ligands, and the π moieties all come from the phenyl groups of the phosphine ligands binding with the Au atoms in the M_{13} core surface. We anticipate that these covalent C–H···π interactions mainly account for the CIEE phenomenon.

The solid-state ^{1}H nuclear magnetic resonance (NMR) analysis (Fig. 7) was then carried out. Both the crystalline state (Fig. 7A) and the amorphous state (Fig. 7B) show two main groups of peaks: 0 to 3.8 parts per million (ppm) corresponding to the H atoms on the alkyl groups of the DPPM ligands ($-CH_2-$) and thiolate ligands ($-CH_3$) and 3.8 to 9.8 ppm for the H atoms on the aryl groups of both DPPM and SR ligands (*52*). Nonetheless, the ^{1}H NMR peaks of the crystalline state are significantly more discrete than those of the amorphous state, indicating that the molecular arrangement in the former case is more organized than that in the latter case.

Powder x-ray diffraction (PXRD) analysis was also performed on the crystalline and amorphous states. According to Fig. 7C, these two states show distinct characteristic peaks. The x-ray diffraction (XRD) curve of the crystalline state is very similar to that of the theoretical one (generated with Mercury 3.0 software; Fig. 7C, inset). Both the $2\theta = 5.5°$ (corresponding to the Miller indices of $10\bar{2}$) and 6.3° (corresponding to the Miller indices of $2\bar{1}0$ and 003) can be clearly identified. Nevertheless, the relative intensity of the second peak was significantly stronger than the theoretical one, presumably because of the slight weathering effect of the crystal under air. By contrast, the prominent peak of $2\theta = 5.5°$ completely disappeared in the XRD

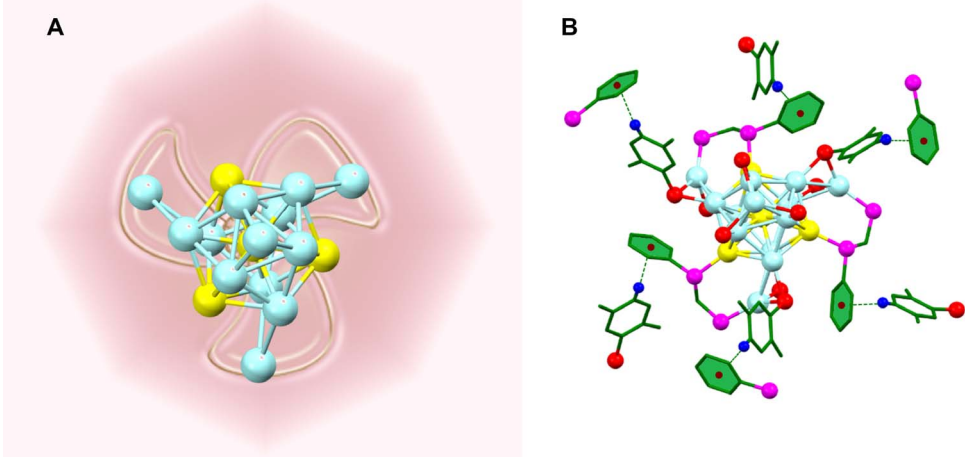

Fig. 6. (**A**) Illustrative diagram for the triblade fan configuration. (**B**) The compact C–H···π interactions in the single crystal.

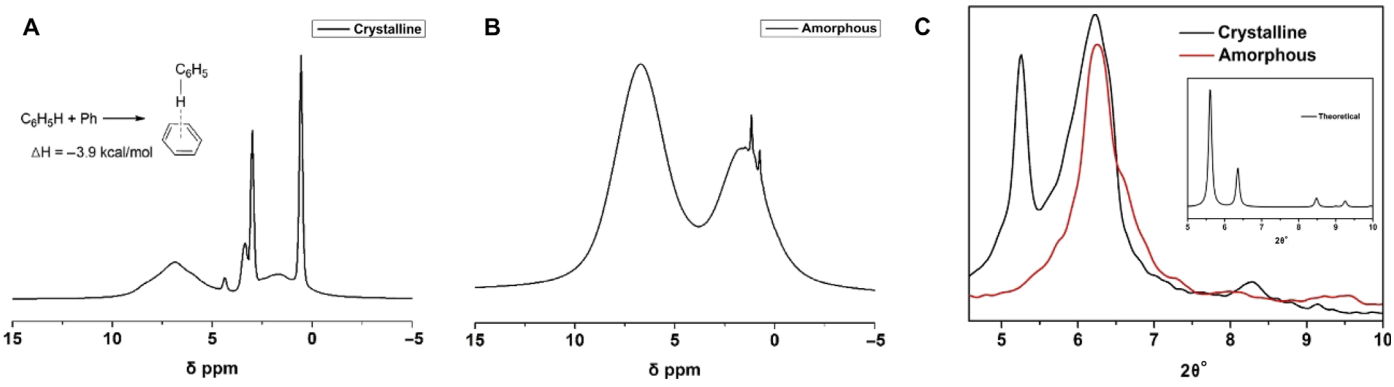

Fig. 7. The solid-state ^{1}H NMR of (**A**) crystalline state and (**B**) amorphous state of Au_4Ag_{13}, and the reaction enthalpy of the C–H···π interaction (A inset). (B) Amorphous state. (**C**) XRD diffractograms for the Au_4Ag_{13} crystalline (black) and amorphous states (red) and theoretical pattern (inset).

curve of the amorphous state, indicating the remarkable change of the crystal lattice. Herein, both the solid-state NMR and the PXRD measurements evidenced the more regular morphology in the crystalline state (compared to the amorphous state). In the more regulated crystalline state, the C–H···π interactions could be better maintained and thus induce stronger luminescence than the amorphous state.

Note that the C–H···π interactions have been frequently observed for macromolecular structures (*53*) and molecular clusters (such as phenyl halide clusters) (*54*–*58*). The H···π distances of 2.8 to 3.1 Å in Au_4Ag_{13} NCs correlate well with the crystallographic packing evidence on the C–H···π interactions previously reported for hexaaryltriindole systems (*59*). Meanwhile, the DFT calculations [with the B3LYP-D3/6-31g(d) method] on the model system (double benzene molecules) also indicate that the formation of these aromatic C–H···π interactions is thermodynamically favored (exothermic by −3.9 kcal/mol; Fig. 7A, inset). The calculations show that the constitution of O–H···π and C–Cl···π (from alcoholic or CH_2Cl_2 solvent) interactions is also feasible (exothermic by 1.8 and 4.8 kcal/mol, respectively). Nonetheless, because of the high regularity of the crystalline state, the weak interactions induced by the tiny amount of solvents could be negligible. However, in the solution phase, the large amount of solvent might disturb the C–H···π interactions of NCs from both the weak interactions and the random collision by the solvent molecules and thus remarkably weakens the luminescence.

CONCLUSION

In summary, a novel bimetallic NC [that is, $Au_4Ag_{13}(DPPM)_3(SR)_9$] was synthesized. An interesting CIEE phenomenon was observed for this structure. In dilute solution and amorphous solid state, the NCs show weak luminescence, whereas in the crystalline state, a strong red emission is observed. According to the structural analysis, solid-state ^{1}H NMR, and the DFT calculations, both the triblade fan configuration of the framework and the multiple weak interactions (that is, C–H···π interactions) contribute to the restriction of the molecular vibrations and rotations, and the latter effect is the determinant for the CIEE (compared to the amorphous state).

MATERIALS AND METHODS

Synthesis of the $Au_4Ag_{13}(DPPM)_3(SR)_9$ NC

The $Au_4Ag_{13}(DPPM)_3(SR)_9$ was synthesized by one-pot method. $AgNO_3$ (34 mg, 0.2 mmol) was first dissolved in 5 ml of methanol. The solution together with 20 mg of $HAuCl_4{\cdot}3H_2O$ (0.05 mmol) and 20 ml of CH_2Cl_2 was then added into the 50-ml three-neck round-bottom flask. The solution was vigorously stirred at room temperature. Then, 50 mg of DPPM and 100 mg of 2,5-dimethylbenzenethiol was added into the mixture, and the solution turned from colorless to white. After about 30 min, 5 ml of $NaBH_4$ aqueous solution (6.0 mg/ml) was quickly added into the solution. The color of the solution immediately turned to black. The reaction was continued for 6 hours, and the raw products were then obtained. From the crude product, the pure crystals were obtained by two steps: raw crystallization and recrystallization. First, the raw $Au_4Ag_{13}(DPPM)_3(SR)_9$ NCs were dissolved in CH_2Cl_2/ether, from which the red crystals were crystallized for about 12 hours. After that, the regular crystal could be obtained by recrystallization in systems such as CH_2Cl_2/ether, CH_2Cl_2/ethanol (1:3), and CH_2Cl_2/hexane (1:3) for 6 hours. For all tests (for example, XPS and UV-vis), the sample crystal was freshly prepared. Detailed descriptions about the materials and characterizations are given in Supplementary Materials and Methods.

SUPPLEMENTARY MATERIALS

Supplementary material for this article is available at http://advances.sciencemag.org/cgi/content/full/3/8/e1700956/DC1

Supplementary Materials and Methods

fig. S1. The overall structure of the Au_4Ag_{13} NC.

fig. S2. The QY of $Au_4Ag_{13}(DPPM)_3(SR)_9$ in CH_2Cl_2 [with the reference $Ru(bipy)_3Cl_2$].

fig. S3. Digital photos of the single-crystal bottle under UV light excitation.

fig. S4. The bright-field image of Au_4Ag_{13} crystals and its fluorescent images under green light excitation (Leica DMI3000 B).

fig. S5. Fluorescence decay profile of the $Au_4Ag_{13}(DPPM)_3(SR)_9$ NCs.

fig. S6. Distances between the hydrogen atom of one thiolate ligand and the centroid of nearby phenyl group of the DPPM ligand.

table S1. Crystal data and structure refinement for the $Au_4Ag_{13}(DPPM)_3(SR)_9$ NC.

REFERENCES AND NOTES

1. J. C. Ma, D. A. Dougherty, The cation-π interaction. *Chem. Rev.* **97**, 1303–1324 (1997).
2. B. Rybtchinski, Adaptive supramolecular nanomaterials based on strong noncovalent interactions. *ACS Nano* **5**, 6791–6818 (2011).
3. H.-J. Schneider, Binding mechanisms in supramolecular complexes. *Angew. Chem. Int. Ed.* **48**, 3924–3977 (2009).
4. C. Zeng, Y. Chen, K. Kirschbaum, K. J. Lambright, R. Jin, Emergence of hierarchical structural complexities in nanoparticles and their assembly. *Science* **354**, 1580–1584 (2016).
5. K. Liu, Y. Kang, Z. Wang, X. Zhang, 25th anniversary article: Reversible and adaptive functional supramolecular materials: "Noncovalent interaction" matters. *Adv. Mater.* **25**, 5530–5548 (2013).

6. G. Liang, L.-T. Weng, J. W. Y. Lam, W. Qin, B. Z. Tang, Crystallization-induced hybrid nano-sheets of fluorescent polymers with aggregation-induced emission characteristics for sensitive explosive detection. *ACS Macro Lett.* **3**, 21–25 (2014).
7. T. J. Morikawa, H. Fujita, A. Kitamura, T. Horio, J. Yamamoto, M. Kinjo, A. Sasaki, H. Machiyama, K. Yoshizawa, T. Ichimura, K. Imada, T. Nagai, T. M. Watanabe, Dependence of fluorescent protein brightness on protein concentration in solution and enhancement of it. *Sci. Rep.* **6**, 22342 (2016).
8. X. Ma, R. Sun, J. Cheng, J. Liu, F. Gou, H. Xiang, X. Zhou, Fluorescence aggregation-caused quenching versus aggregation-induced emission: A visual teaching technology for undergraduate chemistry students. *J. Chem. Educ.* **93**, 345–350 (2016).
9. C. Kumara, C. M. Aikens, A. Dass, X-ray crystal structure and theoretical analysis of $Au_{25-x}Ag_x(SCH_2CH_2Ph)_{18}^-$ alloy. *J. Phys. Chem. Lett.* **5**, 461–466 (2014).
10. Y. Negishi, K. Nobusada, T. Tsukuda, Glutathione-protected gold clusters revisited: Bridging the gap between gold(I)-thiolate complexes and thiolate-protected gold nanocrystals. *J. Am. Chem. Soc.* **127**, 5261–5270 (2005).
11. W. Kurashige, S. Yamazoe, M. Yamaguchi, K. Nishido, K. Nobusada, T. Tsukuda, Y. Negishi, Au_{25} clusters containing unoxidized tellurolates in the ligand shell. *J. Phys. Chem. Lett.* **5**, 2072–2076 (2014).
12. J. Xie, Y. Zheng, J. Y. Ying, Protein-directed synthesis of highly fluorescent gold nanoclusters. *J. Am. Chem. Soc.* **131**, 888–889 (2009).
13. M. Zhu, C. M. Aikens, F. J. Hollander, G. C. Schatz, R. Jin, Correlating the crystal structure of a thiol-protected Au_{25} cluster and optical properties. *J. Am. Chem. Soc.* **130**, 5883–5885 (2008).
14. M. Zhu, C. M. Aikens, M. P. Hendrich, R. Gupta, H. Qian, G. C. Schatz, R. Jin, Reversible switching of magnetism in thiolate-protected Au_{25} superatoms. *J. Am. Chem. Soc.* **131**, 2490–2492 (2009).
15. K. S. Krishna, P. Tarakeshwar, V. Mujica, C. S. S. R. Kumar, Chemically induced magnetism in atomically precise gold clusters. *Small* **10**, 907–911 (2014).
16. J. Yan, H. Su, H. Yang, C. Hu, S. Malola, S. Lin, B. K. Teo, H. Häkkinen, N. Zheng, Asymmetric synthesis of chiral bimetallic $[Ag_{28}Cu_{12}(SR)_{24}]^{4-}$ nanoclusters via ion pairing. *J. Am. Chem. Soc.* **138**, 12751–12754 (2016).
17. M. Zhu, H. Qian, X. Meng, S. Jin, Z. Wu, R. Jin, Chiral Au_{25} nanospheres and nanorods: Synthesis and insight into the origin of chirality. *Nano Lett.* **11**, 3963–3969 (2011).
18. S. Tian, Y.-Z. Li, M.-B. Li, J. Yuan, J. Yang, Z. Wu, R. Jin, Structural isomerism in gold nanoparticles revealed by X-ray crystallography. *Nat. Commun.* **6**, 8667 (2015).
19. X. Kang, L. Xiong, S. Wang, H. Yu, S. Jin, Y. Song, T. Chen, L. Zheng, C. Pan, Y. Pei, M. Zhu, Shape-controlled synthesis of trimetallic nanoclusters: Structure elucidation and properties investigation. *Chem. Eur. J.* **22**, 17145–17150 (2016).
20. G. Wang, R. Guo, G. Kalyuzhny, J.-P. Choi, R. W. Murray, NIR luminescence intensities increase linearly with proportion of polar thiolate ligands in protecting monolayers of Au_{38} and Au_{140} quantum dots. *J. Phys. Chem. B* **110**, 20282–20289 (2006).
21. K. N. Swanick, M. Hesari, M. S. Workentin, Z. Ding, Interrogating near-infrared electrogenerated chemiluminescence of $Au_{25}(SC_2H_4Ph)_{18}^+$ clusters. *J. Am. Chem. Soc.* **134**, 15205–15208 (2012).
22. X.-R. Song, N. Goswami, H.-H. Yang, J. Xie, Functionalization of metal nanoclusters for biomedical applications. *Analyst* **141**, 3126–3140 (2016).
23. S. Wang, X. Meng, A. Das, T. Li, Y. Song, T. Cao, X. Zhu, M. Zhu, R. Jin, A 200-fold quantum yield boost in the photoluminescence of silver-doped Ag_xAu_{25-x} nanoclusters: The 13th silver atom matters. *Angew. Chem. Int. Ed.* **53**, 2376–2380 (2014).
24. A. Das, T. Li, G. Li, K. Nobusada, C. Zeng, N. L. Rosi, R. Jin, Crystal structure and electronic properties of a thiolate-protected Au_{24} nanocluster. *Nanoscale* **6**, 6458–6462 (2014).
25. G. Li, Z. Lei, Q.-M. Wang, Luminescent molecular Ag–S nanocluster $[Ag_{62}S_{13}(SBu^t)_{32}](BF_4)_4$. *J. Am. Chem. Soc.* **132**, 17678–17679 (2010).
26. L. G. AbdulHalim, M. S. Bootharaju, Q. Tang, S. D. Gobbo, R. G. AbdulHalim, M. Eddaoudi, D.-e. Jiang, O. M. Bakr, $Ag_{29}(BDT)_{12}(TPP)_4$: A tetravalent nanocluster. *J. Am. Chem. Soc.* **137**, 11970–11975 (2015).
27. M. S. Bootharaju, C. P. Joshi, M. R. Parida, O. F. Mohammed, O. M. Bakr, Templated atom-precise galvanic synthesis and structure elucidation of a $[Ag_{24}Au(SR)_{18}]^-$ nanocluster. *Angew. Chem. Int. Ed.* **55**, 922–926 (2016).
28. H. Yang, J. Lei, B. Wu, Y. Wang, M. Zhou, A. Xia, L. Zheng, N. Zheng, Crystal structure of a luminescent thiolated Ag nanocluster with an octahedral Ag_6^{4+} core. *Chem. Commun.* **49**, 300–302 (2013).
29. X. Kang, S. Wang, Y. Song, S. Jin, G. Sun, H. Yu, M. Zhu, Bimetallic Au_2Cu_6 nanoclusters: Strong luminescence induced by the aggregation of copper(I) complexes with gold(0) species. *Angew. Chem. Int. Ed.* **55**, 3611–3614 (2016).
30. S. Jin, S. Wang, Y. Song, M. Zhou, J. Zhong, J. Zhang, A. Xia, Y. Pei, M. Chen, P. Li, M. Zhu, Crystal structure and optical properties of the $[Ag_{62}S_{12}(SBu^t)_{32}]^{2+}$ nanocluster with a complete face-centered cubic kernel. *J. Am. Chem. Soc.* **136**, 15559–15565 (2014).
31. N. Goswami, Q. Yao, Z. Luo, J. Li, T. Chen, J. Xie, Luminescent metal nanoclusters with aggregation-induced emission. *J. Phys. Chem. Lett.* **7**, 962–975 (2016).
32. J. Mei, Y. Hong, J. W. Y. Lam, A. Qin, Y. Tang, B. Z. Tang, Aggregation-induced emission: The whole is more brilliant than the parts. *Adv. Mater.* **26**, 5429–5479 (2014).
33. D. Ding, K. Li, B. Liu, B. Z. Tang, Bioprobes based on AIE fluorogens. *Acc. Chem. Res.* **46**, 2441–2453 (2013).
34. X. Cheng, H. Zhang, K. Ye, H. Zhang, Y. Wang, Morphology-dependent fluorescence ON/OFF of a beryllium complex: ACQ in amorphous solids, AEE in crystalline powders and the dark/bright fluorescence switch. *J. Mater. Chem. C* **1**, 7507–7512 (2013).
35. T. Han, X. Feng, D. Chen, Y. Dong, A diethylaminophenol functionalized Schiff base: Crystallization-induced emission-enhancement, switchable fluorescence and application for security printing and data storage. *J. Mater. Chem. C* **3**, 7446–7454 (2015).
36. Y. Dong, J. W. Y. Lam, A. Qin, Z. Li, J. Sun, Y. Dong, B. Z. Tang, Vapochromism and crystallization-enhanced emission of 1,1-disubstituted 2,3,4,5-tetraphenylsiloles. *J. Inorg. Organomet. Polym. Mater.* **17**, 673–678 (2007).
37. L. Qian, B. Tong, J. Shen, J. Shi, J. Zhi, Y. Dong, F. Yang, Y. Dong, J. W. Y. Lam, Y. Liu, B. Z. Tang, Crystallization-induced emission enhancement in a phosphorus-containing heterocyclic luminogen. *J. Phys. Chem. B* **113**, 9098–9103 (2009).
38. Z. Wu, Anti-galvanic reduction of thiolate-protected gold and silver nanoparticles. *Angew. Chem. Int. Ed.* **51**, 2934–2938 (2012).
39. J. Xiang, P. Li, Y. Song, X. Liu, H. Chong, S. Jin, Y. Pei, X. Yuan, M. Zhu, X-Ray crystal structure and optical and electrochemical properties of the $Au_{15}Ag_3(SC_6H_{11})_{14}$ nanocluster with a core–shell structure. *Nanoscale* **7**, 18278–18283 (2015).
40. J. P. Perdew, K. Burke, M. Ernzerhof, Generalized gradient approximation made simple. *Phys. Rev. Lett.* **77**, 3865 (1996).
41. Scientific Computing & Modelling NV, *ADF 2010.01* (Vrije Universiteit, Theoretical Chemistry, 2010).
42. H. Yang, Y. Wang, H. Huang, L. Gell, L. Lehtovaara, S. Malola, H. Häkkinen, N. Zheng, All-thiol-stabilized Ag_{44} and $Au_{12}Ag_{32}$ nanoparticles with single-crystal structures. *Nat. Commun.* **4**, 2422 (2013).
43. Y. Wang, H. Su, C. Xu, G. Li, L. Gell, S. Lin, Z. Tang, H. Häkkinen, N. Zheng, An intermetallic $Au_{24}Ag_{20}$ superatom nanocluster stabilized by labile ligands. *J. Am. Chem. Soc.* **137**, 4324–4327 (2015).
44. Y. Pei, J. Tang, X. Tang, Y. Huang, X. C. Zeng, New structure model of $Au_{22}(SR)_{18}$: Bitetrahederon golden kernel enclosed by $[Au_6(SR)_6]$ Au(I) complex. *J. Phys. Chem. Lett.* **6**, 1390–1395 (2015).
45. Y. Song, J. Zhong, S. Yang, S. Wang, T. Cao, J. Zhang, P. Li, D. Hu, Y. Pei, M. Zhu, Crystal structure of $Au_{25}(SePh)_{18}$ nanoclusters and insights into their electronic, optical and catalytic properties. *Nanoscale* **6**, 13977–13985 (2014).
46. P. J. Hay, W. R. Wadt, *Ab initio* effective core potentials for molecular calculations. Potentials for the transition metal atoms Sc to Hg. *J. Chem. Phys.* **82**, 270 (1985).
47. P. J. Hay, W. R. Wadt, *Ab initio* effective core potentials for molecular calculations. Potentials for K to Au including the outermost core orbitals. *J. Chem. Phys.* **82**, 299 (1985).
48. M. J. Frisch, G. W. Trucks, H. B. Schlegel, G. E. Scuseria, M. A. Robb, J. R. Cheeseman, G. Scalmani, V. Barone, B. Mennucci, G. A. Petersson, H. Nakatsuji, M. Caricato, X. Li, H. P. Hratchian, A. F. Izmaylov, J. Bloino, G. Zheng, J. L. Sonnenberg, M. Hada, M. Ehara, K. Toyota, R. Fukuda, J. Hasegawa, M. Ishida, T. Nakajima, Y. Honda, O. Kitao, H. Nakai, T. Vreven, J. A. Montgomery Jr., J. E. Peralta, F. Ogliaro, M. Bearpark, J. J. Heyd, E. Brothers, K. N. Kudin, V. N. Staroverov, R. Kobayashi, J. Normand, K. Raghavachari, A. Rendell, J. C. Burant, S. S. Iyengar, J. Tomasi, M. Cossi, N. Rega, J. M. Millam, M. Klene, J. E. Knox, J. B. Cross, V. Bakken, C. Adamo, J. Jaramillo, R. Gomperts, R. E. Stratmann, O. Yazyev, A. J. Austin, R. Cammi, C. Pomelli, J. W. Ochterski, R. L. Martin, K. Morokuma, V. G. Zakrzewski, G. A. Voth, P. Salvador, J. J. Dannenberg, S. Dapprich, A. D. Daniels, Ö. Farkas, J. B. Foresman, J. V. Ortiz, J. Cioslowski, D. J. Fox, *Gaussian 09, Revision B.01* (Gaussian Inc., 2009).
49. Y. Dong, B. Xu, J. Zhang, X. Tan, L. Wang, J. Chen, H. Lv, S. Wen, B. Li, L. Ye, B. Zou, W. Tian, Piezochromic luminescence based on the molecular aggregation of 9,10-bis((*E*)-2-(pyrid-2-yl)vinyl)anthracene. *Angew. Chem. Int. Ed.* **51**, 10782–10785 (2012).
50. H. Li, X. Zhang, Z. Chi, B. Xu, W. Zhou, S. Liu, Y. Zhang, J. Xu, New thermally stable piezofluorochromic aggregation-induced emission compounds. *Org. Lett.* **13**, 556–559 (2011).
51. J. Tong, Y. J. Wang, Z. Wang, J. Z. Sun, B. Z. Tang, Crystallization-induced emission enhancement of a simple tolane-based mesogenic luminogen. *J. Phys. Chem. C* **119**, 21875–21881 (2015).
52. I. Schnell, H. W. Spiess, High-resolution ^{1}H NMR spectroscopy in the solid state: Very fast sample rotation and multiple-quantum coherences. *J. Magn. Reson.* **151**, 153–227 (2001).
53. M. Nishio, M. Hirota, Y. Umezawa, *The CH/π Interaction: Evidence, Nature, and Consequences* (Wiley-VCH, 1998).
54. E. M. García-Frutos, G. Hennrich, E. Gutierrez, A. Monge, B. Gómez-Lor, Self-assembly of C_3-symmetrical hexaaryltriindoles driven by solvophobic and CH–π interactions. *J. Org. Chem.* **75**, 1070–1076 (2010).
55. E. Espinosa, I. Alkorta, J. Elguero, E. Molins, From weak to strong interactions: A comprehensive analysis of the topological and energetic properties of the electron density distribution involving X–H···F–Y systems. *J. Chem. Phys.* **117**, 5529–5542 (2002).
56. S. K. Rajagopal, P. S. Salini, M. Hariharan, S···π, π–π, and C–H···π contacts regulate solid state fluorescence in regioisomeric bisthiazolylpyrenes. *Cryst. Growth Des.* **16**, 4567–4573 (2016).

57. S. Sarkhel, A. Rich, M. Egli, Water–nucleobase "stacking": H–π and lone pair–π interactions in the atomic resolution crystal structure of an RNA pseudoknot. *J. Am. Chem. Soc.* **125**, 8998–8999 (2003).
58. C. R. Forbes, S. K. Sinha, H. K. Ganguly, S. Bai, G. P. A. Yap, S. Patel, N. J. Zondlo, Insights into thiol–aromatic interactions: A stereoelectronic basis for S–H/π interactions. *J. Am. Chem. Soc.* **139**, 1842–1855 (2017).
59. A. L. Ringer, M. S. Figgs, M. O. Sinnokrot, C. D. Sherrill, Aliphatic C–H/π interactions: Methane–benzene, methane-phenol, and methane–indole complexes. *J. Phys. Chem. A* **110**, 10822–10828 (2006).

Acknowledgments
Funding: We acknowledge financial support from the National Natural Science Foundation of China (21372006, 21631001, 21672001, and U1532141), the Ministry of Education, the Education Department of Anhui Province, and the 211 Project of Anhui University. **Author contributions:** T.C. and Y.S. synthesized the NCs and analyzed the crystals. T.C., S.Y., J.C., and J.F. carried out the property measurements (including the optical and structural analysis). T.C. and B.R. carried out the theoretical calculations. H.S. was responsible for synthesis and crystallization. H.Y. was responsible for property characterization and theoretical calculations. M.Z. was responsible for the design of the project. All authors contributed to the writing of the manuscript and the data analysis. **Competing interests:** The authors declare that they have no competing interests. **Data and materials availability:** All data needed to evaluate the conclusions in the paper are present in the paper and/or the Supplementary Materials. Additional data related to this paper may be requested from the authors.

Submitted 15 April 2017
Accepted 13 July 2017
Published 18 August 2017
10.1126/sciadv.1700956

Citation: T. Chen, S. Yang, J. Chai, Y. Song, J. Fan, B. Rao, H. Sheng, H. Yu, M. Zhu, Crystallization-induced emission enhancement: A novel fluorescent Au-Ag bimetallic nanocluster with precise atomic structure. *Sci. Adv.* **3**, e1700956 (2017).